Toward Quantitative Whole Organ Thermoacoustics With a Clinical Array Plus One Very Low-Frequency Channel Applied to Prostate Cancer Imaging

Sarah K. Patch, *Member, IEEE*, David Hull, William A. See, and George W. Hanson, *Fellow, IEEE*

***Abstract*—Thermoacoustics has the potential to provide quantitative images of intrinsic tissue properties, most notably electrical conductivity in Siemens/meter, much as shear wave elastography provides tissue stiffness in kilopascal. Although thermoacoustic imaging with optical excitation has been commercialized for small animals, it has not yet made the transition to clinic for whole organ imaging in humans. The purpose of this work was to develop and validate specifications for a clinical ultrasound array for quantitative whole organ thermoacoustic imaging. Imaging a large organ requires exciting thermoacoustic pulses throughout the volume and broadband detection of those pulses because tomographic image reconstruction preserves frequency content. Applying the half-wavelength limit to a 200-μm inclusion inside a 7.5-cm diameter organ requires measurement sensitivity to frequencies ranging from 4 MHz to 10 kHz, respectively. A dual-transducer system utilizing a P4-1 array connected to a Verasonics V1 system as well as a focused single-element transducer sensitive to lower frequencies was developed. Very high-frequency (VHF) irradiation generated thermoacoustic pulses throughout a $6 \times 6 \times 5$ cm^3 volume. In the VHF regime, electrical conductivity drives thermoacoustic signal production. Simultaneous acquisition of thermoacoustic pulses by both transducers enabled comparison of transducer performance. Data from the clinical array generated a stack of 96 images with a separation of 0.3 mm, whereas the single-element transducer imaged only in a single plane. In-plane resolution and quantitative accuracy were quantified at isocenter. The array provided volumetric imaging capability with superior resolution whereas the single-element transducer provided superior quantitative accuracy in axial images. Combining axial images from both transducers preserved resolution of the P4-1 array and improved image contrast. Neither transducer was sensitive to frequencies below 50 kHz, resulting in a dc offset and low-frequency shading over fields of view exceeding 15 mm. Fresh human prostates were imaged *ex vivo* and volumetric reconstructions reveal structures rarely seen in diagnostic images. In conclusion, quantitative whole-organ thermoacoustic tomography will be feasible by sparsely interspersing transducer elements sensitive to the low end of the ultrasonic range.**

***Index Terms*—Medical imaging, medical signal and image processing, photoacoustics, prostate cancer imaging, system and device design.**

I. Introduction

THERMOACOUSTICS has the potential to join quantitative imaging techniques such as X-ray CT and shear wave elastography that provide images representing tissue density and stiffness, respectively. Thermoacoustic images represent an induced pressure jump in Pascals from which intrinsic tissue properties can be inferred. When very high-frequency (VHF) irradiation is used, thermoacoustic pulse amplitudes are most closely correlated to electrical conductivity. Thermoacoustic imaging is an inverse acoustic source problem, in which a broadband thermoacoustic pulse travels from internal source to external detector that passively records the thermoacoustic pulse in receive-only mode. Challenges to thermoacoustic imaging over large fields of view are the ability to generate detectable thermoacoustic pulses throughout large volumes and adequate receive chain bandwidth. The first challenge can be overcome by irradiating with VHF [1] or ultra high-frequency [2] irradiation. In the following, we demonstrate that a clinical ultrasound array augmented with the addition of one element sensitive to very low frequencies can overcome the challenge of receiver bandwidth. Combining data from a clinical array with 1–4-MHz sensitivity band with lower frequency single-element transducer measurements preserve resolution of the P4-1 images and improves quantitative accuracy.

To the best of the authors' knowledge, the results presented in the following are novel in two aspects. Precisely because VHF radiation penetrates deep into soft tissue, electromagnetic energy loss and thermoacoustic signal generation are weak compared to photoacoustics. Our lab is the first to use a clinical ultrasound array to detect VHF-induced thermoacoustic pulses that have traveled through 45 mm or more of soft tissue. Furthermore, this is the first report of quantitative imaging of VHF-induced thermoacoustic measurements, which required augmenting the clinical ultrasound receiver with a single-element transducer sensitive to frequencies below 1 MHz.

Thermoacoustics shares features of ultrasound tomography techniques, although there are significant differences. Both have long histories and have generated more results than can be cited, so only a few early papers are mentioned here. Ultrasound tomography was introduced in the 1970s [3], [4] and discussed in a review of diagnostic tomography techniques

Manuscript received May 5, 2015; accepted December 22, 2015. Date of publication December 29, 2015; date of current version January 26, 2016. This work was supported in part by the UW-Milwaukee Intramural Instrumentation Grant and in part by NIH CTSA Award #8UL1TR000055.

S. K. Patch is with the Department of Physics, UW-Milwaukee, Milwaukee, WI 53211 USA (e-mail: patchs@uwm.edu).

D. Hull is with Avero Diagnostics, Irving, TX 75039 USA (e-mail: dhull@averodx.com).

W. A. See is with the Department of Urology, Medical College of Wisconsin, Milwaukee, WI 53226 USA (e-mail: wsee@mcw.edu).

G. W. Hanson is with the Department of Electrical Engineering, UW-Milwaukee, Milwaukee, WI 53211 USA (e-mail: george@uwm.edu).

Digital Object Identifier 10.1109/TUFFC.2015.2513018

0885-3010 © 2015 IEEE. Personal use is permitted, but republication/redistribution requires IEEE permission.
See http://www.ieee.org/publications_standards/publications/rights/index.html for more information.

including ultrasound, X-ray, and emission tomography in 1979 [5]. Biomedical thermoacoustic imaging was introduced in the early 1980s [6]–[8]. Ultrasound pulse-echo and diffraction tomography require scattering that is generally neglected in thermoacoustics. Attenuation and time-of-flight ultrasound tomographic techniques that neglect scattering convert travel time and decreased pulse amplitude to line integrals of "slowness" and attenuation coefficient. Spherical integrals of the thermoacoustic source may be inferred from time-of-flight of thermoacoustic pulses. Reconstruction of a function from its line integrals is well studied for biomedical application, and forms the basis of X-ray computerized tomography. Reconstruction of a function from its spherical integrals is required for both thermoacoustics and also diffraction tomography when the same transducer transmits and receives [9]. When reconstructing a function from its line integrals, care must be taken when filtering low-frequency components to avoid low-frequency shading across the image [5]. Accurately representing low-frequency spherical Radon data are also critical for thermoacoustic tomography, but require more than a software fix, as discussed in the following.

A thermoacoustic pulse propagates according to the inhomogeneous linear acoustic wave equation, assuming constant soundspeed ν_s and zero initial conditions

$$\left[\frac{\partial^2}{\partial t^2} - \nu_s^2 \Delta\right] p(\mathbf{x}, t) = S(\mathbf{x})\, I'(t). \tag{1}$$

The source $S(\mathbf{x})$ is a power density and I is the dimensionless temporal envelope of a short- and high-power electromagnetic irradiation pulse that causes a rapid pressure jump. In microwave and VHF-induced thermoacoustics, $S(\mathbf{x}) = \Gamma\sigma(\mathbf{x})\left|\mathbf{E}(\mathbf{x})\right|^2$, where Γ is the dimensionless Grueneisen, which is assumed as constant. $\mathbf{E}(\mathbf{x})$ is the electric field and $\sigma(\mathbf{x})$ is the total conductivity, which includes frequency-independent ionic conductivity and relaxation effects [10]. Electrical conductivity can be recovered by dividing the initial pressure jump by $\Gamma\left|\mathbf{E}(\mathbf{x})\right|^2 \int_{R^1} I(t)\, dt$.

Long wavelengths tend to penetrate deeper and with more uniformity than short wavelengths, in both electromagnetic and mechanical regimes. Electromagnetic irradiation at 100 MHz has 3-m wavelength in vacuum and wavelength exceeding 30 cm in soft tissue. Therefore, a homogeneous electric field can be assumed over a quarter wavelength, or 75 mm. In fact, MRI coils surrounding the patient propagate circularly polarized VHF magnetic fields with parts-per-million homogeneity into the adult abdomen. The results presented below were obtained by irradiating fresh human prostates immersed in 0.2 M glycine solution with an 11-kV/m TE10 incident field, which more closely approximates plane wave irradiation. As shown in Appendix I, the applied electric field is reflected somewhat at the tissue–glycine interface, reducing the **E**-field strength to 8 kV/m inside a 5-cm diameter specimen and 6 kV/m inside a 1-cm diameter cylindrical phantom. However, **E**-field homogeneity is excellent because the electromagnetic wavelength is long compared to the dimensions of the prostate. Homogeneity of the incident **E**-field is a strength of VHF-induced thermoacoustics over microwave and optical regimes in which the **E**-field [11] and optical fluence vary rapidly. Because optical fluence decreases rapidly with imaging depth, a plethora of results have been reported for quantitative photoacoustics, as reviewed in [12]. A numerical feasibility study at 8 GHz demonstrated the need for sophisticated electromagnetic modeling due to the rapid absorption and short wavelength of the electric field [13]. Quantitative VHF-induced thermoacoustic imaging of fresh surgical prostate specimens is presented below.

VHF-induced thermoacoustics has the potential to quantify electrical conductivity σ, which may provide value clinically. For instance, prostatic fluids are primarily produced in the peripheral zone (PZ) and healthy prostates produce exceedingly high levels of the anion citrate [14]. To maintain electrochemical balance, cation concentration elevates in response, resulting in high overall ionic content [15]. Decreased citrate production suppresses overall ion concentration, electrical conductivity, and VHF-induced thermoacoustic signal strength.

Multiple factors impact the bandwidth of measured VHF-induced thermoacoustic pulses: electromagnetic irradiation pulsewidth, directivity and frequency response of the ultrasonic measurement hardware, and of course, the object itself. Assuming an omnidirectional passive receiver, thermoacoustic measurements are represented mathematically as

$$p_{\text{meas}}(\mathbf{x}, t) = (p_{\text{ideal}} * I * h)(\mathbf{x}, t)$$

where convolution is performed with respect to time. p_{ideal} represents pressures generated by an impulsive excitation in which $I(t) = \delta(t)$ and h is the frequency response of the ultrasound receive hardware (both transducer and electronics). The irradiation pulse I applies a low-pass filter with essential bandlimit of the main lobe given by 1/pulsewidth, whereas the receive hardware applies a bandpass filter. Optical pulsewidths used in photoacoustics are on the order of 10 ns, whereas microwave and VHF pulsewidths are typically on the order of a microsecond. Low-pass limits on photoacoustic and VHF-induced thermoacoustic pulses are therefore typically on the order of 100 and 1 MHz, respectively. Additionally, spectral content of thermoacoustic pulses is negatively correlated with electromagnetic depth penetration [16], because acoustic attenuation further reduces high-frequency content of thermoacoustic pulses that travel several centimeters through soft tissue. Electromagnetic depth penetration is greater in the VHF regime than in the near infrared regime used for photoacoustics. For these reasons, power spectra of signals generated during whole organ thermoacoustic imaging are overwhelmingly low frequency. Although recovering small inclusions and discontinuities at tissue interfaces requires generating and detecting high-frequency signal, accurately recovering pixel values of the source term $S(x)$ requires sensitivity to low-frequency content. Quantitative thermoacoustic imaging therefore hinges upon the high-pass limit imposed by the receive chain, rather than low-pass limits.

Section II contains a brief analysis comparing k-space content of thermoacoustic and transmission tomography images. Section III presents the methods and materials that are used to characterize a benchtop thermoacoustic tomography system and image fresh surgical prostate specimens. Section IV contains reconstructions of the initial pressure jump in Pascals, and also rescaled to represent electrical conductivity in Siemens/meter. A discussion in Section V is followed by a brief conclusion.

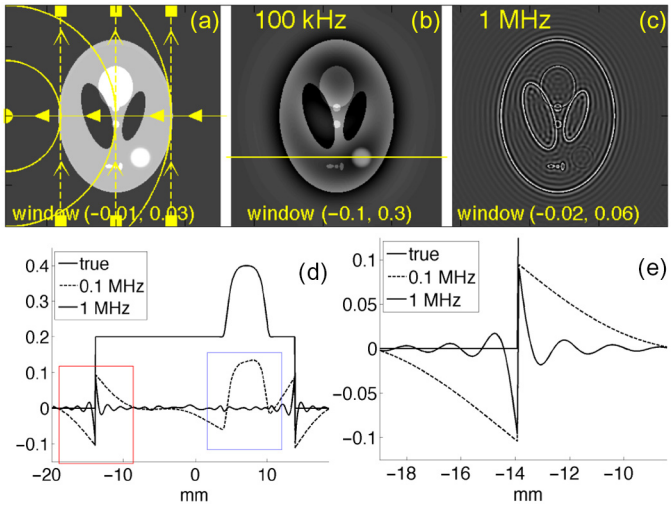

Fig. 1. Modified Shepp–Logan phantom. (a) True image. Yellow circle indicates a transducer that passively records thermoacoustic pulses; yellow squares indicate pairs of transducers operating in pitch-catch mode for ultrasound tomography. Filtered images with high-pass limits of (b) 0.1 and (c) 1 MHz. (d) Profiles along horizontal yellow line in (b) through diffuse mass. (e) Red box indicates region plotted; and blue box includes diffuse mass.

II. Thermoacoustic versus Ultrasound Transmission Tomography

To analyze the impact of bandlimitations on thermoacoustic images, we note that the frequency, or k-space, content of the thermoacoustic source is related to frequency content of measured thermoacoustic pulses, as analyzed in [17]

$$\begin{aligned}&\mathbf{F}h\left(f\right)\mathbf{F}I\left(f\right)\mathbf{F}S\left(\mathbf{k}\right)\\&\quad=\left(\frac{iC_p}{k\beta}\right)\int\limits_{\mathbf{y}\in\Omega}\mathbf{n}\cdot\left[\nabla\mathbf{F}p_{\text{meas}}\left(\mathbf{y},f\right)\right.\\&\qquad\left.+\,i\mathbf{k}\mathbf{F}p_{\text{meas}}\left(\mathbf{y},f\right)\right]e^{-i\mathbf{k}\cdot\mathbf{y}}dS_{\mathbf{y}}\\&\quad=\mathbf{F}S_{\text{meas}}\left(\mathbf{k}\right)\end{aligned}\tag{2}$$

where $\mathbf{F}$ represents the Fourier transform with Fourier variable, k and $k=|\mathbf{k}|=f/\nu_s$.$\mathbf{n}$ is the outward unit normal to the measurement surface Ω, which surrounds the field of view. Integration is performed with respect to the variable $\mathbf{y}\in\Omega$. Finally, thermal properties of the tissue are specific heat capacity C_p and expansivity β. Image reconstruction may be performed by series expansions [18], filtered backprojection [19], [20], or time reversal, which is efficiently implemented in k-space [21]. In any case, (2) directly relates bandlimitations of the reconstructed image S_{meas} to bandlimitations imposed by the irradiation pulse I, ultrasound receive chain h, and frequency content of the true image S. p_{meas} is bandlimited from above by all three functions h, I, and S. FI achieves its maximum at 0 Hz, so S_{meas} is high-pass limited only by h and S. In Fig. 1(a), a transducer indicated by a large yellow circle passively records a time series representing integrals of the thermoacoustic source over spheres indicated by thick arcs. Fourier transforming this time series yields $\mathbf{F}p_{\text{meas}}$. Equation (2) shows that each k-space component in $\mathbf{F}S_{\text{meas}}\left(\mathbf{k}\right)$ is a weighted average of $\mathbf{F}p_{\text{meas}}\left(\mathbf{y},\nu_s k\right)$ over transducer locations $\mathbf{y}$ on and near the measurement surface.

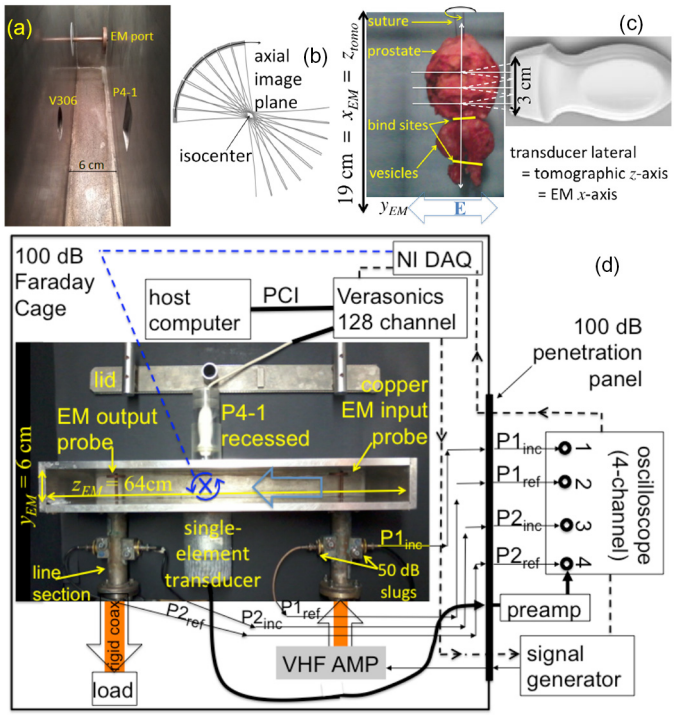

Fig. 2. Hardware configuration. (a) View along length of testbed. Single-element and P4-1 transducers are positioned in the circular and rectangular ports, respectively. (b) Axial reconstruction plane in reference frame of object. Nominal region of elevational sensitivity depicted by gray lines for multiple tomographic views as the transducer rotates about center. (c) Transducer orientation relative to tomographic z-axis and TE x-axis. Each transducer element corresponds to a tomographic reconstruction slice. The **E**-field polarization is parallel to the transducer axis. (d) Schematic with the aerial view of testbed into which the prostate is suspended. The tomographic z-axis indicated by a blue "×" is perpendicular to the page.

The classic half-wavelength resolution limit and soundspeed $\nu_s = 1.5$ mm/μs imply that a system with an upper bandlimit of 4 MHz can recover inclusions as small as 190 μm. Applying the same rule of thumb to recovery of background values of a 75-mm diameter object requires sensitivity to the audible frequency of 10 kHz, which is the very low end of the ultrasound frequency range.

III. Methods and Materials

Data were collected in a benchtop system that is an electromagnetic waveguide along which 700-ns electromagnetic pulses propagated to initiate thermoacoustic imaging. The 700-ns pulsewidth essentially bandlimited I to 1.4 MHz, with first sidelobe covering (1.4, 2.8) MHz. Thermoacoustic emissions were bandlimited similarly. Single element and phased array ultrasound transducers positioned on either side of the testbed as in Fig. 2(a) simultaneously detected thermoacoustic generated by a specimen suspended in between. Data sets are analogous to sinograms acquired in step-and-shoot fashion by X-ray computerized tomography scanners, but represent integrals over spheres rather than straight lines. Although the specimen rotates in the testbed, the position and elevational sensitivity of an element in the P4-1 array are depicted in the frame of the specimen in Fig. 2(b).

Conventions for coordinate axes of waveguides, tomography systems, and transducer arrays require clarification. Standard transverse electric $\mathrm{TE}_{m,n}$ waveguides propagate traveling waves along a horizontal z-axis. $\mathrm{TE}_{m,n}$ waveforms have *m* and *n* half-wavelengths along horizontal *x* and vertical *y* directions, respectively. The **E**-field in a conventional TE_{10} waveguide is polarized vertically, but our system is rotated by 90°, so that the **E**-field is polarized horizontally. Electric field strength is zero at the top and bottom of the waveguide, and is maximal at midheight, where the transducers are positioned. The transducer's lateral axis is oriented vertically, as shown in Fig. 2(c). The specimen is suspended below a stepper motor that rotates and translates the specimen about a vertical axis, indicated by an "×" in Fig. 2(d). *In vivo,* this vertical axis would be parallel to the superior–inferior (SI) direction along the patient's spine. In this thermoacoustic computerized tomography (TCT) system, we follow the convention that the axis of translation and rotation is the vertical z-axis. In summary, the tomographic z-axis is the x-axis of the TE_{10} waveguide and the lateral direction along the transducer array.

The measurement aperture was cylindrical, similar to that of third-generation X-ray CT systems. Traditional ultrasound beamforming sums data from many neighboring transducer channels and reconstructs an image in the plane defined by the array. Reconstructing a volume requires additional data.

Therefore, thermoacoustic projections were collected at multiple tomographic view angles as the specimen rotated 360° about the vertical tomographic axis, which was parallel to the lateral axis of the transducer [Fig. 2(c)]. The single-element transducer collected one sinogram, while the P4-1 array collected a stack of sinograms.

In an effort toward quantitative reconstruction of the pressure jump induced by EM irradiation, single-element measurements were normalized so that image pixel values represent Pascals. Frequency response of the P4-1 array and Verasonics V1 receive chain, i.e., transducer elements and electronics, have not been measured. Because sinograms were acquired simultaneously, P4-1 results are therefore scaled to have the same L^2-norm as the single element results.

Image reconstruction was performed by filtered backprojection. Volumetric backprojection consists of summing the results of delay-and-sum beamforming over all view angles. In this work, 21 neighboring channels were used in beamforming at each of 200 tomographic view angles. Clinical arrays are focused in the elevational direction and provide high resolution along the transducer axis with reduced lateral resolution. High sampling rates correspond to high resolution along the transducer axis in B-mode imaging and provided good in-plane resolution.

A schematic of the entire system, with photo of the imaging testbed embedded is shown in Fig. 2(d). Thick solid lines denote data cables that transmit thermoacoustic pulses, thin solid lines represent coaxial cables that transmit VHF pulses, and thick dashed lines represent communication cables. The VHF amplifier, testbed, and V1 ultrasound system were housed inside 100-dB Faraday cage (ETS Lindgren).

A. Ultrasound Hardware: Single Element and Multichannel

A 96 channel P4-1 (ATL) ultrasound transducer array was located directly opposite to a focused videoscan single-element transducer (Olympus V306) as shown in Fig. 2(a) and (d). The transducers received thermoacoustic pulses simultaneously, and passively recorded sinograms that were 180° out of phase. Although their specified center frequencies of 2.25 and 2.5 MHz were similar, the single element receive chain was more sensitive to frequencies below 1 MHz than that of the P4-1 array and V1 receive electronics, as discussed in the following.

1) Verasonics Hardware: A Verasonics V1 system and 96-channel P4-1 array detected thermoacoustic pulses in receive-only mode. The P4-1 element width is 0.245 mm with a pitch of 0.295 mm. The array was oriented with axis parallel to the **E-**field and rotated laterally to provide nearly 3 cm coverage along the tomographic z-axis of rotation and translation.

Because thermoacoustic pulses are broadband compared to ultrasound pulse echoes, the receive-only sampling frequency was set to 30 MHz, threefold higher than the nominal 10-MHz rate set by Verasonics for a P4-1 array.

Despite 43.5-dB amplification, 1024 signals were averaged to reduce noise. To minimize signal loss due to software filtering, preprocessing that is normally performed on pulse echo ultrasound data before transferring to the host computer was eliminated.

The P4-1 array was positioned with the transducer face flush with the vertical testbed wall, exposed to the full strength of the applied electric field, which exceeded 10 kV/m. Although the piezoelectric transducer acts as an antenna and is sensitive to the electric field, the Verasonics V1 receive electronics suppressed electromagnetic interference (EMI). The V1's input signal range is 1.6 V peak-to-peak. At higher voltages, the input diodes conduct and keep the input to the receiver at safe levels. EMI detected by the P4-1 probe has not damaged these diodes and receiver recovery time has been less than 3 μs, providing excellent EMI suppression.

2) Single Element Hardware: Single element sinograms were collected simultaneously, much as described in [22]. The 2.25-MHz transducer has 1.27-cm diameter and 2.03-cm focal distance and is specified to have 100% bandwidth around a center frequency of 2.25 MH, i.e., a sensitivity band of 1.1–3.4 MHz. Early system characterization, however, quantified transducer response to be on the order of $1\ \mu\mathrm{V/Pa}$ with surprisingly flat frequency response from 100 kHz to 4 MHz, but with strong notches near the specified upper and lower bandlimits [23]. Signals were carried to the penetration panel by a doubly shielded waterproof cable (Olympus BCU-58-6-DSW). A low-noise preamplifier (Olympus 5662) amplified by 54 dB. The 512 signals were averaged on the oscilloscope (Tektronix DPO 7104) before recording to disk.

B. Phantoms: Resolution and Contrast

Two different phantoms representing different source terms $S(\mathbf{x})$ were utilized to characterize the system. An $80\text{-}\mu\mathrm{m}$ copper wire represented a line source with high-frequency content in-plane. Thermoacoustic emissions from 1-cm diameter

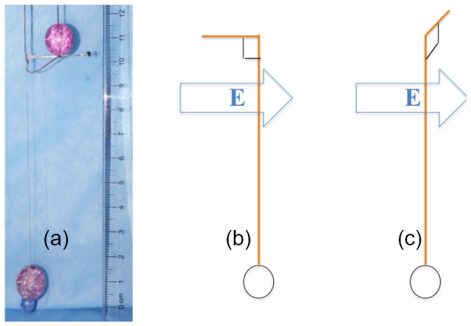

Fig. 3. Orientation of **E** versus horizontal crossbar of in-plane resolution phantom. (a) Photo of the phantom. (b) Horizontal crossbar is parallel to **E**-field, which drives current flow. (c) **E**-field is perpendicular to both horizontal and vertical sections, so no current is induced.

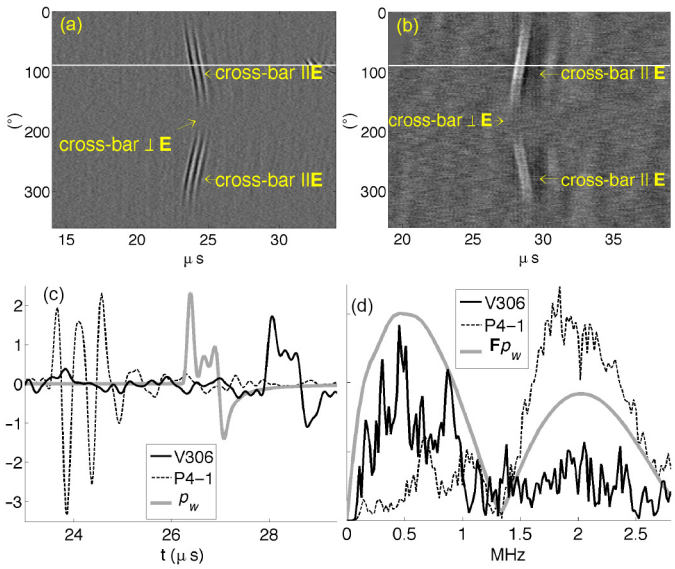

Fig. 4. In-plane resolution sinograms, pulses, and spectra. Sinograms from (a) P4-1 and (b) single-element transducers with orientation of the upper crossbar indicated. White horizontal lines indicate the projections plotted in (c) that have spectra plotted in (d). Black lines indicate measurements of the thermoacoustic emission from the wire. Gray lines indicate the modeled data that are time shifted for convenience of display.

contrast phantoms were lower frequency than those from the wire phantom, but broadband compared to emissions from the prostate specimens imaged.

1) Resolution Phantom: The in-plane point spread function (PSF) was quantified at isocenter by imaging a simple phantom made from 12.5 cm of 80-μm diameter copper wire shown in Fig. 3. One end of the flexible copper wire was affixed to a 2.5-cm length of stiff 500-μm aluminum, which was suspended horizontally in the testbed. The remaining 10 cm of copper wire hung along the tomographic z-axis, weighted by glass beads. The vertical copper segment remained within 500 μm of the z-axis throughout tomographic data acquisition, well within the elevational sensitivity region of the P4-1 array.

Polarization effects caused the signal to wax and wane as the phantom rotated near isocenter, as shown in Fig. 4. The applied electric field was horizontally polarized, and therefore no current was induced in the vertical wire. When the horizontal crossbar rotated into alignment with the electric field, current was induced along the horizontal wire and carried to the vertical section of the copper wire, producing a thermoacoustic pulse.

Thermoacoustic emissions from the vertical copper wire can be modeled analytically, and the resulting thermoacoustic pulses are closely related to the applied irradiation pulse $I(t)$. Either D'Alembert's method of descent or simply solving (1) when $S(\mathbf{x}) = \delta(\mathbf{x})$ and integrating the solution along the axis of the wire yields a formula for thermoacoustic pulses generated by an infinite wire p_w. Working in cylindrical coordinates, with $r = \sqrt{x^2 + y^2}$ representing distance to the wire

$$p_w(r,t) = \frac{1}{4\pi}\int_{z\in\boldsymbol{R}} \frac{I'\left(t - \sqrt{r^2+z^2}/\nu_s\right)}{\sqrt{r^2+z^2}} dz = \left[I^* g_w\right](r,t) \tag{3}$$

where $g_w(r,t) = \mathrm{Re}\left(\frac{t}{2\pi(t^2 - r^2/\nu_s^2)^{3/2}}\right)$ and the convolution is carried out with respect to time. g_w approximates a delta function and the shape of p_w is closely related to the irradiation pulse I.

Thermoacoustic measurements are additionally bandlimited by the transducers' receive sensitivity. Thermoacoustic pulses indicated by white horizontal lines on the sinograms were measured simultaneously and are compared to the modeled pulse p_w in Fig. 4(c). Measured and modeled spectra are compared in Fig. 4(d). Black solid and dashed lines indicate data measured by the single element and clinical array, respectively, whereas thick gray lines indicates the modeled pulse. p_w was modeled according to (3) using a measured VHF pulse envelope I as described in Appendix II. In Fig. 4(d), the null at 1.4 MHz in $\mathbf{F}p_w$ agrees with nulls in the spectra measured by both transducers. Although the single-element (V306) transducer is advertised to have a center frequency of 2.25 MHz, the single element receive chain detected lower frequencies in the main lobe of $\mathbf{F}p_w$. The clinical array and V1 receive electronics, however, was more sensitive to the first sidelobe. Neither accurately detected frequencies below 100 kHz, so a high-pass filter was applied.

2) Contrast Phantom: Plastic drinking straws of different radii filled with physiologic saline were used to quantify contrast. Each straw was cut to 10-cm length, and a glass bead was affixed to one end using waterproof sealant. The straw was then filled with 0.9% physiologic buffered saline solution and an identical glass bead was affixed to the top end of the straw. Care was taken to avoid trapping air beneath the topmost bead. These contrast phantoms were suspended vertically in the testbed, perpendicular to both E-field polarization and propagation directions. The largest straw for which the single element reconstructions provided good contrast was nearly circular, with long and short axes of approximately 12 and 11 mm.

C. Prostate Specimens

Twelve fresh prostate specimens were imaged immediately after surgical resection performed as a part of routine care for biopsy-confirmed prostate cancer. Informed consent was obtained from all subjects in accordance with the local institutional review board. Specimen handling was performed as

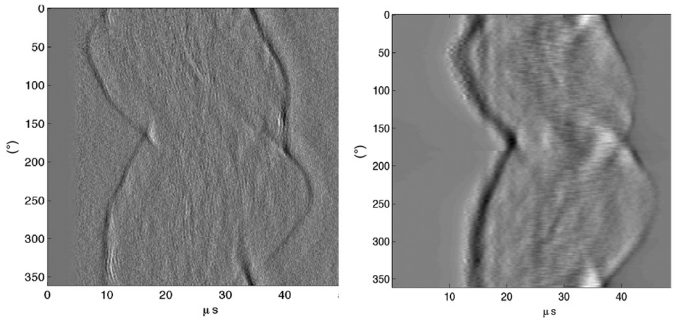

Fig. 5. Corrected and filtered sinograms collected by channel 51 on the P4-1 array (left) and single-element transducer (right). Single-element sinogram shifted by 180° for the sake of visual comparison.

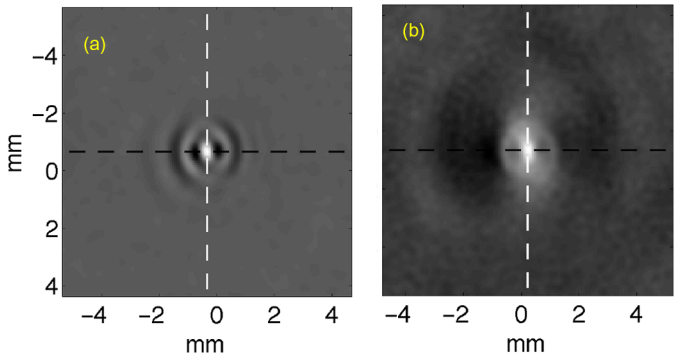

Fig. 6. In-plane PSFs from channel 49 of (a) array and (b) single-element transducer.

described in [22], except that scanning was performed faster, due to the large number of channels in the P4-1 array which provided nearly 3 cm coverage along the z-axis. Prostates were scanned at room temperature within a 90-min time window rather than in chilled acoustic couplant over a 4-h time window. Sinograms displayed in Fig. 5 were acquired simultaneously, but the single-element sinogram has been shifted 180° for ease of comparison. Signal from the back edge of the prostate is clearly visible in each sinogram, traveling for $30\ \mu\text{s}-45\ \text{mm}$ through the thickest aspect of the gland.

D. Data Acquisition

Data acquisition was driven by LabVIEW software. Prior to acquiring thermoacoustic data, incident and reflected VHF pulses were acquired to monitor electromagnetic system performance. For each tomographic view, a trigger was sent to the Verasonics system, initiating acquisition of the next tomographic view. The Verasonics system then transmitted TTL triggers to a signal generator (Rohde-Schwarz SML01), initiating thermoacoustic signal generation and acquisition. The MATLAB script driving the Verasonics system is straightforward because the P4-1 array did not transmit, but only received thermoacoustic pulses. Thermoacoustic signals were weak and signal averaging was required to reduce noise. A 1024 thermoacoustic pulses were generated at a rate of 250 Hz; acquisition time was approximately 4 s/view. All 1024 pulses were summed by the V1 system, and single element data were captured simultaneously. Between views a dual-motion stepper motor (Haydon-Kerk, DCM-8028) rotated 1.8° in 64 microsteps; positioning time was approximately 2 s/view. Additional time was required for LabVIEW communication and data storage, resulting in a 25-min acquisition time for a 200-view sinogram.

E. TCT Image Reconstruction

Image reconstruction was performed offline via filtered backprojection after data correction. Both P4-1 and single element data were bandpass filtered with kernels smoothed over ± 50-kHz intervals about the (100 kHz and 4 MHz) bandpass limits. Reconstruction of the P4-1 measurements was performed by quasi-volumetric backprojection of data from the 21 neighboring channels. Only two slices of single element data were collected before and after 20-mm translation. Therefore, single element data were backprojected in-plane.

To capture the broadest bandwidth possible, raw Verasonics V1 data were accessed prior to filtering. The most significant systematic error in raw V1 data is channel-to-channel offset, which is normally corrected in software using a 21-tap (bandpass) FIR filter prior to beam forming. Offsets were removed using calibration data collected immediately after acquiring image data. The suture by which the specimen is suspended was cut, and the specimen sank to the bottom of the testbed. It was well out of range of the transducers (6–8 cm below) while calibration data were collected. Subtracting calibration data removed channel-to-channel offsets.

Approximate values for the electric field strength and integral of the pulse envelope are derived in Appendices I and II, respectively. Results below assume $\int_{R^1} I(t)dt = 600$ ns and 8 and 6 kV/m for the electric field strength inside a 5-cm prostate and 1-cm cylindrical contrast phantom, respectively. Applying the Gruneisen of water $\Gamma = 0.1$ to prostatic tissue yields conductivity-to-Pascals scaling factors $0.1(8\ \text{kV/m})^2\ 600\ \text{ns} = 3.8\ \text{Pa}/\left(\text{Siemens}/m\right)$ in prostates and $0.1(6\ \text{kV/m})^2\ 600\ \text{ns} = 2.2\ \text{Pa}/\left(\text{Siemens}/m\right)$ in saline-filled straws.

IV. Results

Pixel values in single element images below represent Pascals and electrical conductivity, based upon direct measurements of single element receive chain sensitivity and the conversion factors derived in Appendix II. Black numbers above colorbars indicate Pascals; maximum and minimum electrical conductivities are written near either end of the colorbars in Figs. 7 and 8.

A. Resolution

Reconstruction of sinograms in Fig. 4 yields oblong, rather than radial PSFs. The PSFs are visibly sharper in the direction parallel to the **E**-field, than in the direction perpendicular to the **E**-field. White and black lines in Fig. 6 represent these directions. Full-width at half-maximum (FWHM) are reported in Table I.

TABLE I
FWHMS OF 80-μm WIRE

Cross-bar orientation	V306+preamp (μm)	P4-1+V1 (μm)
parallel	500	250
perpendicular	1125	438

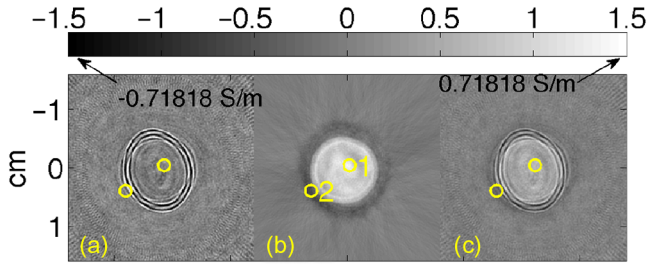

Fig. 7. Images of 1-cm diameter saline-filled straw from (a) P4-1 data, (b) single-element data, and (c) averaged.

TABLE II
CONTRAST PHANTOM CONDUCTIVITY

ROI #	Averaged (S/m)	Single element (S/m)	P4-1 (S/m)
σ_1	0.29 ± 0.04	0.56 ± 0.08	0.03 ± 0.09
σ_2	−0.08 ± 0.12	−0.22 ± 0.10	0.07 ± 0.20
$\sigma_1 - \sigma_2$	0.37	0.78	−0.04

B. Contrast

Images of the largest saline-filled straw for which good contrast were obtained by the single-element transducer are shown in Fig. 7. Mean and standard deviations of electrical conductivity inside the yellow circles are reported in S/m in Table II. Pixel values were averaged over 195 points within each yellow circle. Values for the P4-1 array are effectively zero. Just as the 100-kHz high-pass limit accurately recovered the size of jumps in the numerical phantom, the difference between average values inside and just outside the straw in the single element image yield electrical conductivity of 0.79 Siemens/meter, which is within 20% of the true value for physiologic saline at 100 MHz [24], [25].

C. Thermoacoustic Images of Fresh Human Prostates

Axial images of specimen #1 are compared and contrasted to analyze transducer performance in Figs. 8 and 9. Additionally, axial as well as reformatted sagittal and coronal reformats from P4-1 data are presented in Fig. 10 for two additional specimens. Only two sinograms of single element data were acquired, at a separation of 2 cm but two overlapping stacks of P4-1 sinograms are acquired. The P4-1 data set therefore yielded a stack of 162 sinograms and reconstruction slices at z-locations defined by the P4-1 elements, whereas the single element data provided only two slices of each prostate. Sinograms that generated the images in Fig. 8(a)–(c) were acquired during the first rotation, and are reconstructed at the z-position defined by the single-element detector and middle channels of the P4-1

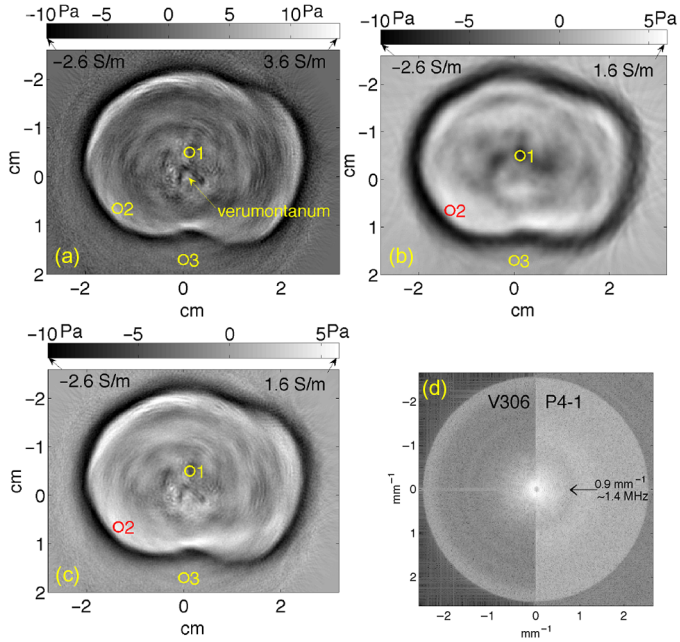

Fig. 8. Reconstructions from (a) P4-1 and (b) single-element measurements. (c) Average of the images in (a) and (b). (d) k-space comparison of the images in (a) and (b), displayed on the same log scale.

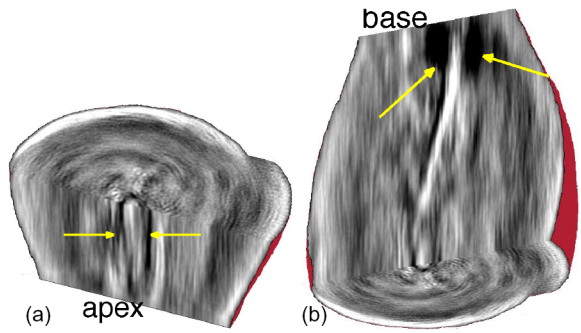

Fig. 9. Specimen #1. Visualization of the volumetric reconstruction from P4-1 data displaying a coronal slice and the anterior portion of the axial slice in Fig. 8(a). (a) Compressed urethra indicated by yellow arrows descends toward the apex. (b) Seminal vesicles indicated by yellow arrows.

array. Volumetric visualization and reformatting in Fig. 10 were performed using 3-D Slicer [26].

Both images in Fig. 8(a) and (b) are bandpassed representations of the induced pressure jump, which is nonnegative. However, high-pass filtering imposed by h, the frequency response of receive transducer and electronics, results in aphysical negative reconstruction values throughout much of the specimen. Averaging the images much as was done in [27] and [28] increases bandwidth and reduces the fraction of negative pixel values inside the prostate as seen in Fig. 8(c), to create an image with increased bandwidth. All reconstructed images are real valued, with Hermitian symmetric Fourier transforms. To compare frequency content of the individual images in Fig. 8(a) and (b), left and right halves of k-space are compared in Fig. 8(d).

In each image, three regions of interest (ROIs) are selected corresponding to regions of signal dropout (#1), enhancement

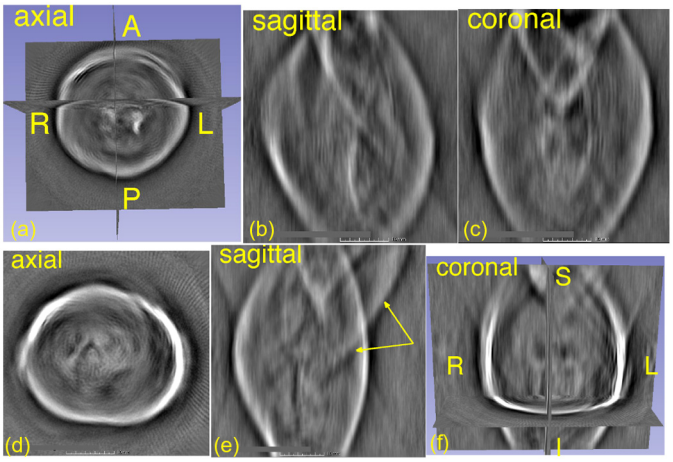

Fig. 10. Specimens #2 and #3. Reformatted images from clinical array data. Images of specimen #2 in (a)–(c) reveal ductal structure. Specimen #3 (d)–(f) had engorged vesicles, indicated by yellow arrows in (d).

TABLE III
CONDUCTIVITY IN PROSTATE

ROI #	Averaged (S/m)	Single Element (S/m)	P4-1 (S/m)
σ_1	-0.97 ± 0.38	-1.68 ± 0.21	-0.26 ± 0.61
σ_2	1.19 ± 0.13	0.94 ± 0.25	1.43 ± 0.34
σ_3	-0.01 ± 0.09	-0.06 ± 0.07	0.03 ± 0.16
$\sigma_2 - \sigma_1$	2.16	2.62	1.69

TABLE IV
SNR IN PROSTATE

ROI #	Combined Reconstruction	Single Element	P4-1
1	2.5	8.1	0.4
2	9.0	3.8	4.2

(#2), and background (#3). Estimates of electrical conductivity inside each ROI are presented in Table III; SNR for ROIs #1 and #2 is reported in Table IV.

Although SNR of the single element image is greater magnitude than in the P4-1 image, the single element image in Fig. 8(b) has insufficient resolution to capture the wedge-shaped verumontanum that is clearly displayed in the P4-1 image in Fig. 8(a). Additionally, both images in Fig. 8(a) and (b) contain large regions of aphysical negative values. The combined image preserves the resolution of the P4-1 image and regions of aphysical negative reconstruction values are reduced in the combined image.

The P4-1 image displayed in Fig. 8(a) provides context for coronal cuts through the volume in Fig. 9(a) and (b), which were reconstructed from P4-1 data alone, because the single-element transducer captured only two slices. The compressed urethra is visualized by black streaks descending toward the apex of the prostate. Dark spots visible on either side, near the base of the prostate, represent portions of the seminal vesicles.

Fig. 10 contains reformatted images of additional specimens reconstructed from data collected with the clinical array alone.

V. DISCUSSION

Volumetric reconstructions in Figs. 9 and 10 are encouraging because they were acquired by a clinical array and visualize structures that are not commonly seen in current diagnostic images. Fig. 10 demonstrates the feasibility of performing VHF-induced thermoacoustic imaging with clinical arrays, but Fig. 8 demonstrates the need to incorporate a few low-frequency elements onto the form factor of a clinical array in order to image quantitatively. All images were reconstructed from signal containing zero energy below 50 kHz, which corresponds to the low energy circle of radius 0.033 1/mm in the middle of k-space in Fig. 8(d). Fifty kilohertz also corresponds to a half-wavelength of 15 mm, and reasonably uniform contrast was obtained by the single-element transducer in a homogeneous phantom of 1-cm cross section, but aphysical negative image values were obtained in larger phantoms and midglands of prostate specimens, which have diameter exceeding 3 cm. Therefore, jumps at the prostate–glycine interface in single element images accurately reflect induced pressure within approximately 1 cm of the prostate–glycine boundary, just as the 100-kHz high-pass limit led to visualization of the diffuse lesion despite inaccurate recovery of background tissue values in Fig. 1(b). The system is designed to recover diffuse lesions of 1-cm diameter, but cannot expect to detect gradual changes in electrical conductivity over larger regions. Truly quantitative whole organ imaging will require incorporating elements with sensitivity to frequencies in the audible regime, below 20 kHz.

Applying an electric field that is polarized only in the y-direction and qualitatively normalizing P4-1 data to have the same L^2-norm as single element data are weaknesses of this study. The 11-kV/m incident field failed to fully penetrate into the contrast phantom, resulting in an internal field of less than 6 kV/m. Applying a field with variable polarization will be critical *in vivo*. Even after accounting for diminished E-field penetration, reconstructions of the saline-filled plastic drinking straws have jumps of less than 0.8 S/m at the straw boundary. This underestimates the 1 S/m measured electrical conductivity of physiologic saline at 100 MHz [25]. However, low-permittivity plastic straws are not as well matched to glycine solution as prostatic tissue. Images of prostate specimens routinely have jumps of 10–15 Pa at the prostate–glycine interface, indicating electrical conductivity of 2–4 S/m in the periphery of the prostate, which is consistent with the elevated electrical conductivity of prostatic fluid. If the frequency response of the P4-1 + Verasonics receive electronics were known, frequency content of the combined image could be optimized in software [29].

In vivo imaging will require optimization of electromagnetic hardware to improve bandwidth and minimize polarization effects. Resolution of the P4-1 images is higher than that of the single element images, and is limited by the applied EM irradiation pulse I. The 4-MHz bandpass limit applied by the P4-1 array implies an optimal 190-μm resolution, but the PSF from the P4-1 has a best-case FWHM of 250 μm, corresponding to the 2.8-MHz null of the first sidelobe of the irradiation PSD.

Although the 2.8-MHz null is not clearly visible in the k-space image in Fig. 9 (right), the 1.4-MHz null between main and first sidelobe appears as a dark ring with radius $0.9\,\mathrm{mm}^{-1}$.

The limited measurement aperture available for *in vivo* imaging may present the greatest challenge to VHF-induced thermoacoustic imaging of the prostate. Biplane transrectal ultrasound (TRUS) probes provide several 5–6 cm of linear coverage, whereas end-fire TRUS probes have radius of curvature less than 1 cm, and therefore provide less than 2 cm coverage in any orientation, but can be rotated to provide a hemispherical measurement aperture. Methods to increase the effective measurement aperture by utilizing multiple scattering are well studied for both electromagnetics (radar) and acoustics (sonar and ultrasound). Utilizing strong reflectors to synthetically increase the measurement aperture has also been applied to thermoacoustics [30]–[34].

VI. Conclusion

This work demonstrates feasibility of whole-organ VHF-induced thermoacoustic imaging using clinical arrays. Quantitative thermoacoustic imaging will be possible using a calibrated receive chain that includes some transducer elements sensitive to frequencies at the high end of the audible range.

Appendix I
EM Modeling

Electromagnetic scattering due to spherical and cylindrical objects is easily modeled with harmonic expansions. To model the situation in our testbed, we revert to the standard EM coordinate system and follow the treatment in [35]. A 11-kV/m incident **E**-field is polarized in the *x*-direction and propagates along the z-axis; the E_x component is considered below. A 5-cm diameter sphere representing a prostate and 1-cm diameter cylinder of physiologic saline are immersed in deionized water mixed with 15-g/L glycine powder. The dielectric properties of glycine solutions have been studied in the VHF regime, but properties of prostatic tissue have not been reported. A relative permittivity of 0.2 M glycine solution at room temperature has been reported ranging from $78 - 10j$ [36] to $90.35 - 0.1j$ [37], with negligible conductivity due to ionic content. We model the spectrum of prostatic tissue using the relative permittivity of heart muscle but the electrical conductivity of blood and plasma. A four term Cole–Cole model for heart tissue has a relative permittivity at 100 MHz of $\varepsilon_{\mathrm{heart}} = 91 - 132\ j$ with conductivity due to ionic content of only $\sigma_{\mathrm{heart}} = 0.1\ \mathrm{S/m}$ [38]. Overall ionic content of prostatic fluid produced by diseased glands is at least that of blood and plasma, but resides primarily in the posterior PZ. Therefore, we assume average conductivity due to ionic content of $\sigma_i = 0.7\ \mathrm{S/m}$, resulting in an overall permittivity for the prostate of

$$\varepsilon_{\mathrm{prostate}} = \varepsilon_{\mathrm{heart}} - j\frac{\sigma_i}{2\pi f \epsilon_o} = \varepsilon_r' + j\frac{\sigma_{\mathrm{tot}}}{2\pi f \epsilon_o} = 91 - 249j.$$

Total conductivity σ_{tot} accounts for loss due to relaxation effects as well as ionic content, which contribute nearly equally to power loss in this model. In other words, total conductivity, $\sigma_{\mathrm{tot}} = 1.39\ \mathrm{S/m}$,is approximately twice that due to ionic content alone.

Results below assume $\varepsilon_{\mathrm{gly}} = 78 - 10\ j$, which is poorly matched to $\varepsilon_{\mathrm{prostate}}$, so the results represent a conservative estimate of **E**-field strength and homogeneity. Although the real components of relative permittivity are similar (78 versus 91), the difference in the imaginary components (10 versus 249) results in higher electromagnetic energy loss within the prostate than the glycine solution and causes significant reflection at the glycine–prostate boundary. In Fig. 11(a), profiles along the x- and y-axis through the center of the sphere reveal excellent field homogeneity inside the sphere. A linear gradient along the z-axis is due to attenuation as the wave propagates. E_x is shown in the *xz* plane in Fig. 11(b), with the rotation of the specimen indicated by yellow arrows. Inhomogeneity along the z-axis is averaged over the course of a 360° rotation. E_x in the *yz* and *xy* planes is shown in Fig. 11(c) and (d), respectively. Evaluating E_x at points on a spherical lattice inside the 5-cm diameter sphere yields a mean $\mu = 7.9\ \mathrm{kV/m}$ and standard deviation of only $\sigma = 30\ \mathrm{V/m}$.

We therefore assume uniform electric field strength *inside* the specimen, despite strong field inhomogeneity just outside of the prostate near the x-axis. Additionally, E_x is lower inside the specimen than in the surrounding glycine solution.

Physiologic saline is designed to mimic the ionic content of blood and plasma and its dielectric properties are well known. Stogryn's model yields $\varepsilon_{\mathrm{PBS}} = 75.2 - 272j$ at 100 MHz [24], which agrees with more recent measurements [25]. The sidewalls of the plastic straws used to generate data in Table II and Fig. 7 were less than $200\ \mu\mathrm{m}$ thick, and were neglected in our numerical models. A 1-cm diameter cylinder with complex permittivity of physiologic saline oriented perpendicular to both propagation and polarization directions experiences a weaker internal **E**-field than the sphere with dielectric properties of prostatic tissue. Modeling in the cylindrical straw phantom was performed using software [39] that follows the conventions in [35]. E_x is plotted along both polarization and propagation directions in Fig. 11(e). The electric field is homogeneous inside the straw, but is weaker than inside the prostate, averaging only 5.9 kV/m.

Appendix II
EM Measurements and Pascals-to-Conductivity Scaling

Electromagnetic design and validation of a larger testbed for imaging porcine kidneys can be found in [40]. A brief summary of electromagnetic aspects that bandlimit thermoacoustic pulses and impact the relationship between induced pressure in Pascals and electrical conductivity in Siemens per meter follows.

About–10-dBm pulses with a carrier frequency of 108 MHz and 700-ns pulsewidth were transmitted through a penetration panel to a custom pulsed amplifier (QEI VHF50KP), which amplified them to 20-kW peak power and 15-kV/m electric field strength. A $50 - \Omega$ rigid copper coaxial line transmits these high-power pulses to the imaging testbed. Incident and reflected power are monitored at both input and output ports of

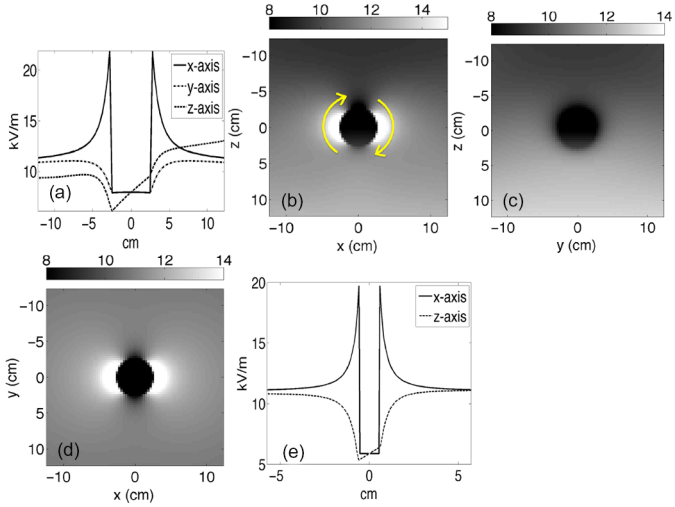

Fig. 11. Harmonic expansions of $E\mathbf{x}$. Colorbars represent kV/m. (a)–(d) Pertain to a 5-cm sphere. (e) Pertains to a 1-cm diameter cylinder. (a) Profiles of $E\mathbf{x}$ inside sphere. (b)–(d) $E\mathbf{x}$ in the (b) *xz* plane of rotation, (c) *yz* plane, and (d) *xy* plane. (e) Profiles of $E\mathbf{x}$ inside cylinder.

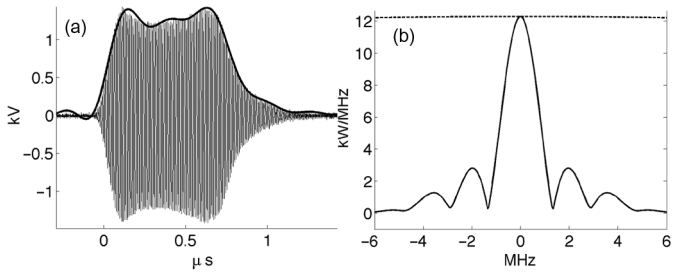

Fig. 12. (a) Voltage of incident EM pulse (thin) and square root of the pulse envelope I (thick). (b) PSD of incident pulses of width 700 and 10 ns.

the testbed using $50-\Omega$ directional coupler line sections outfitted with 50-dB attenuating slugs (Bird, 4715, and 4274) to measure voltage. An incident pulse plotted in Fig. 12(a) can be modeled by

$$V(t) = V_{\max} \sin(\omega_o t) \sqrt{I(t)}$$

where ω_o is the carrier frequency of 108 MHz. Instantaneous power at the coaxial testbed port is given by $P(t) = V^2(t)/\Omega$. Averaging over a cycle (approximately 10 ns) yields

$$P(t) = \left(V_{\max}^2/2\Omega\right) I(t)$$

where the dimensionless pulse envelope I is nonnegative and achieves a maximum value of one. The pulse shown in Fig. 12(a) had $V_{\max} = 1.42$ kV, and $\int_{R^1} I(t)\,dt = 607$ ns. Therefore, $12.3\ \text{mJ} = \int P(t)\,dt$ propagated toward the testbed. Reflected power was approximately 10%, so 11 mJ propagated along the waveguide toward the specimen.

The Fourier transform of $P(t)$ is referred to as the power spectral density (PSD) and is essentially bandlimited to 1.4 MHz ($= 1/700$ ns). A normalized PSD of a 10-ns optical pulse is flat over the frequency range of diagnostic ultrasound transducers, shown by the dashed line in Fig. 12(b).

ACKNOWLEDGMENT

The authors would like to thank Dr. K. Jacobsohn and M. Yang, Y. Qadadha, and I. Elsharef for procuring fresh prostate specimens and collecting data. They would also like to thank R. Daigle, C. Crawford, and anonymous referees for their helpful comments and suggestions, and the MCW tissue bank, R. Navarro, and H. Engelke, RN, for staff support.

REFERENCES

[1] A. Eckhart, R. Balmer, W. See, and S. Patch, "Ex vivo thermoacoustic imaging over large fields of view with 108 MHz irradiation," *IEEE Trans. Biomed. Eng.*, vol. 58, no. 8, pp. 2238–2246, Aug. 2011.

[2] Y. Fu, Z. Ji, W. Ding, F. Ye, and C. Lou, "Thermoacoustic imaging over large field of view for three-dimensional breast tumor localization: A phantom study," *Med. Phys.*, vol. 41, p. 110701, Nov. 2014.

[3] J. Greenleaf, S. Johnson, S. Lee, G. Herman, and E. Wood, "Algebraic reconstructions of spatial distributions of acoustic absorption within tissue from their two-dimensional acoustic projections," in *Proc. 5th Int. Symp. Acoust. Hologr. Imag.*, Palo Alto, CA, 1973, pp. 591–604.

[4] J. Greenleaf, S. Johnson, W. Samayoa, and F. Duck, "Algebraic reconstruction of spatial distributions of acoustic velocities in tissue from their time-of-flight profiles," in *Proc. 6th Int. Symp. Acoust. Hologr.*, 1975, pp. 71–90.

[5] A. C. Kak, "Computerized tomography with X-ray, emission, and ultrasound sources," *Proc. IEEE*, vol. 67, no. 9, pp. 1245–1272, Sep. 1979.

[6] T. Bowen, "Radiation-induced thermoacoustic soft tissue imaging," presented at the IEEE Ultrasonics Symposium, Chicago, IL, 1981.

[7] F. Caspers and J. Conway, "Measurement of Power Density in a Lossy Material by means of Electromagnetically induced acoustic signals for non-invasive determination of spatial thermal absorption in connection with pulsed hyperthermia," presented at the 12th European Microwave Conference, Helsinki, Finland, 1982.

[8] J. C. Lin and K. H. Chan, "Microwave thermoelastic tissue imaging-system design," *IEEE Trans. Microw. Theory Tech.*, vol. 32, no. 8, pp. 854–860, Aug. 1984.

[9] S. Norton and M. Linzer, "Ultrasonic reflectivity imaging in three dimensions: Reconstruction with spherical transducer arrays," *Ultrason. Imaging*, vol. 1, pp. 210–239, 1979.

[10] C. Gabriel, S. Gabriely, and E. Corthout, "The dielectric properties of biological tissues: I. Literature survey," *Phys. Med. Biol.*, vol. 41, pp. 2231–2249, 1996.

[11] X. Wang, D. R. Bauer, R. Witte, and H. Xin, "Microwave-induced thermoacoustic imaging model for potential breast cancer detection," *IEEE Trans. Biomed. Eng.*, vol. 59, no. 10, pp. 2782–2791, Oct. 2012.

[12] B. Cox, J. Laufer, S. Arridge, and P. Beard, "Quantitative spectroscopic photoacoustic imaging: A review," *J. Biomed. Opt.*, vol. 17, p. 061202, 2012.

[13] L. Yao, G. Guo, and H. Jiang, "Quantitative microwave-induced thermoacoustic tomography," *Med. Phys.*, vol. 37, pp. 3752–9, Jul. 2010.

[14] L. C. Costello and R. B. Franklin, "Prostatic fluid electrolyte composition for the screening of prostate cancer: A potential solution to a major problem," *Prostate Cancer Prostatic Dis.*, vol. 12, pp. 17–24, 2009.

[15] J. P. Kavanagh, "Sodium, potassium, calcium, magnesium, zinc, citrate and chloride content of human prostatic and seminal fluid," *J. Reprod. Fertil.*, vol. 75, pp. 35–41, Sep. 1985.

[16] J. Liu, C. Wei, Y. Sheu, Y. Tasi, Y. Wang, and P.-C. Li, "Design, fabrication and testing of a dual-band photoacoustic transducer," *Ultrason. Imag.*, vol. 30, pp. 217–227, 2008.

[17] M. Anastasio, J. Zhang, D. Modgil, and P. J. La Rivière, "Application of inverse source concepts to photoacoustic tomography," *Inverse Prob.*, vol. 23, pp. S21–S36, 2007.

[18] S. J. Norton and M. Linzer, "Ultrasonic reflectivity imaging in three dimensions: exact inverse scattering solutions for plane, cylindrical, and spherical apertures," *IEEE Trans. Biomed. Eng.*, vol. BME-28, no. 2, pp. 202–220, Feb. 1981.

[19] D. Finch, S. K. Patch, and Rakesh, "Determining a function from its mean values over a family of spheres," *SIAM J. Math. Anal.*, vol. 35, pp. 1213–1240, 2003.

[20] M. Xu and L. V. Wang, "Universal back-projection algorithm for photoacoustic computed tomography," *Phys. Rev. E*, vol. 71, p. 016706, 2005.

[21] B. E. Treeby and B. T. Cox, "k-Wave: MATLAB toolbox for the simulation and reconstruction of photoacoustic wave-fields," *J. Biomed. Opt.*, vol. 15, p. 021314, 2010.
[22] S. Patch, D. Hull, M. Thomas, S. Griep, K. Jacobsohn, and W. See, "Thermoacoustic contrast of prostate cancer due to heating by very high frequency irradiation," *Phys. Med. Biol.*, vol. 60, pp. 689–708, 2015.
[23] D. Pachauri, T. Stiles, N. Purwar, P. Dey, and S. Patch, "Transducer frequency response and impact on TPOAT signal," presented at the SPIE BIOS, Photons Plus Ultrasound, San Jose, 2008.
[24] A. Strogryn, "Equations for calculating the dielectric constant of saline water," *IEEE Trans. Microw. Theory Tech.*, vol. 19, no. 8, pp. 733–736, Aug. 1971.
[25] M. Stoneman *et al.*, "Correction of electrode polarization contributions to the dielectric properties of normal and cancerous breast tissues at audio/radiofrequencies," *Phys. Med. Biol.*, vol. 52, pp. 6589–6604, 2007.
[26] A. Fedorov *et al.*, "3D Slicer as an image computing platform for the quantitative imaging network," *Magn. Reson. Imaging*, vol. 30, pp. 1323–1341, Nov. 2012.
[27] G. Ku, X. Wang, G. Stoica, and L. V. Wang, "Multiple-bandwidth photoacoustic tomography," *Phys. Med. Biol.*, vol. 49, pp. 1329–1338, 2004.
[28] J. Gateau, A. Chekkoury, and V. Ntziachristos, "Ultra-wideband three-dimensional optoacoustic tomography," *Opt. Lett.*, vol. 38, pp. 4671–4674, Nov. 8, 2013.
[29] P.-C. Li, C.-W. Wei, and Y.-L. Sheu, "Subband photoacoustic imaging for contrast improvement," *Opt. Express*, vol. 16, pp. 20215–20226, 2008.
[30] D. Wu, X. Wang, C. Tao, and X. Liu, "Limited-view photoacoustic tomography utilizing backscatterers as virtual transducers," *Appl. Phys. Lett.*, vol. 99, p. 244102, 2011.
[31] D. Wu, C. Tao, and X. Liu, "Photoacoustic tomography in scattering biological tissue by using virtual time reversal mirror," *J. Appl. Phys.*, vol. 109, p. 084702, 2011.
[32] R. Ellwood, E. Zhang, P. Beard, and B. Cox, "Photoacoustic imaging using acoustic reflectors to enhance planar arrays," *J. Biomed. Opt.*, vol. 19, p. 126012, 2014.
[33] B. Cox, S. Arridge, and P. Beard, "Photoacoustic tomography with a limited-aperture planar sensor and a reverberant cavity," *Inverse Prob.*, vol. 23, pp. S95–S112, 2007.
[34] L. Kunyansky, B. Holman, and B. Cox, "Photoacoustic tomography in a rectangular reflecting cavity," *Inverse Prob.*, vol. 29, p. 125010, 2013.
[35] C. Bohren and D. Huffman, *Absorption and Scattering of Light by Small Particles*. Hoboken, NJ, USA: Wiley, 1983.
[36] K. Kumar, S. Bhaumik, T. Vishwam, V. Subramanian, and V. Murthy, "Dielectric relaxation behaviour of glycine in aqueous solution medium in the microwave frequency region," *Indian J. Eng. Mater. Sci.*, vol. 15, pp. 196–198, 2008.
[37] R. B. Talwarea, P. G. Hudgea, Y. S. Joshia, and A. C. Kumbharkhanea, "Dielectric relaxation study of glycine–water mixtures using time domain reflectometry technique," *Phys. Chem. Liq. Int. J.*, vol. 50, pp. 102–112, 2011.
[38] S. Gabriel, R. W. Lau, and C. Gabriel, "The dielectric properties of biological tissues: III. Parametric models for the dielectric spectrum of tissues," *Phys. Med. Biol.*, vol. 41, pp. 2271–2293, 1996.
[39] J. Schäfer, S. Lee, and A. Kienle, "Calculation of the near fields for the scattering of electromagnetic waves by multiple infinite cylinders at perpendicular incidence," *J. Quant. Spectrosc. Radiat. Transfer*, vol. 113, pp. 2113–2123, 2012.
[40] D. Fallon, L. Yan, G. W. Hanson, and S. K. Patch, "RF testbed for thermoacoustic tomography," *Rev. Sci. Instrum.*, vol. 80, p. 064301, 2009.

Sarah K. Patch, (M'04) photograph and biography not available at the time of publication.

David Hull photograph and biography not available at the time of publication.

William A. See photograph and biography not available at the time of publication.

George W. Hanson, (S'85–M'91–SM'98–F'09) photograph and biography not available at the time of publication.